



HAL
open science

Volume Assessment of the Cerebrospinal Fluid Spaces for Computer Aided Diagnosis

Alain Lebet, Eric Petit, Bruno Durning, Jérôme Hodel, Philippe Decq, Alain
Rahmouni

► **To cite this version:**

Alain Lebet, Eric Petit, Bruno Durning, Jérôme Hodel, Philippe Decq, et al.. Volume Assessment of the Cerebrospinal Fluid Spaces for Computer Aided Diagnosis. 2011. hal-00638369

HAL Id: hal-00638369

<https://hal.science/hal-00638369>

Preprint submitted on 4 Nov 2011

HAL is a multi-disciplinary open access archive for the deposit and dissemination of scientific research documents, whether they are published or not. The documents may come from teaching and research institutions in France or abroad, or from public or private research centers.

L'archive ouverte pluridisciplinaire **HAL**, est destinée au dépôt et à la diffusion de documents scientifiques de niveau recherche, publiés ou non, émanant des établissements d'enseignement et de recherche français ou étrangers, des laboratoires publics ou privés.

Volume Assessment of the Cerebrospinal Fluid Spaces for Computer Aided Diagnosis

A. Lebret, E. Petit, B. Durning, J. Hodel, A. Rahmouni and P. Decq

October 25, 2011

Abstract

The present work aims to provide support in the diagnosis of hydrocephalus, which requires an assessment to the volumes of the cerebrospinal fluid (CSF) within its total, ventricular and subarachnoid spaces. In this paper we describe a fully automatic method to estimate the CSF volumes from a new 3D whole body MR imaging sequence. The method was developed using image properties as well as anatomical and geometrical features, completed with a topological assumption on the CSF shape. Experiments on phantoms and clinical data were performed and evaluated by comparing our assessments of volumes with those derived from a segmentation controlled by expert physicians. Then we show that a robust distinction between pathological cases and healthy adult people can be achieved by a linear discriminant analysis on volumes of the ventricular and intracranial subarachnoid spaces. We also find that healthy adults maintain a proportional relationship between these volumes.

Keywords: cerebrospinal fluid, hydrocephalus, 3D segmentation, topology preservation, computer-aided diagnosis

1 Introduction

Hydrocephalus is caused by an abnormal accumulation of the cerebrospinal fluid (CSF) into cerebral ventricles and/or subarachnoid cisterns of the brain (see [23] for more details). Obviously the measurement of mechanical features such as CSF pressures or volumes may be of great interest for assisted diagnosis and therapeutic [21, 16].

As MRI is a reference technique for the CSF imaging, a new sequence that significantly highlights the CSF, has recently been developed for intracranial images [9] and is also tested for whole body images. Due to the poor dynamic of the luminance perception of the human visual system, such images appear to be binary but in fact they are not (see Fig. 3, 4), and furthermore they are disturbed by noise and artifacts.

For now, the volume assessment of the CSF spaces is achieved by expert physicians by extracting the total volume through thresholding and interactive removal of noise and unwanted structures. Next, this volume is separated into its ventricular, spinal and intracranial subarachnoid spaces. This leads to a functional parameter calculated by the ratio between the ventricular CSF space volume and the intracranial subarachnoid one. This ratio could be efficient to discriminate healthy adults from patients affected by an hydrocephalus. However, it should be pointed out that most of the previous steps used to be manually performed and that the overlapping of ratio ranges between healthy people and patients may result to misclassification.

In order to solve these problems, we first propose to fully automate the above segmentation and separation steps, and then to refine the classification by applying a linear discriminant

analysis to the ventricular and intracranial subarachnoid CSF volumes. We also show that healthy adults maintain a proportional relationship between these volumes.

To solve the segmentation and separation problems, we do not only use image properties, but also anatomical and geometrical features as well as a topological assumption about the CSF shape. The topological assumption becomes necessary because of both, the complex geometry of the CSF shape as shown in Fig. 1 (left), and the numerous image artifacts (especially motion artifacts), which can lead to changes in its topology. Benefits of associating topological constraints to medical image segmentation methods are shown in [29]. These constraints may prevent from any change in the topology of the anatomical structures to be extracted, such as unwanted created connections and/or holes. From a topological point of view, each anatomical structure including the CSF may be considered as a simple object such as a filled or a hollow sphere [1, 20, 25]. Several works have successfully added such constraints to their approach in order to preserve the topology of anatomical objects throughout the segmentation process (deformable surface with an energy minimization goal [18, 22], level set [8], fast marching [1], discrete deformable model [20], morphological operators [5, 25], statistical and topological atlases registration approach [2]).

Here, from a topological point of view, the CSF space is considered as a filled sphere as shown in Fig. 1 (right). This property, used as a refinement constraint, brings both accuracy and robustness to our segmentation method.

The paper is organized as follows. Section 2 describes the segmentation methodology for the whole CSF. The separation of the CSF volume into its ventricular, intracranial and spinal subarachnoid sub-volumes is presented in section 3. In section 4, we report experiments on phantoms and clinical dataset. Concluding remarks are given in section 5.

2 Segmentation of the whole CSF

The total CSF volume is segmented by using image properties with the hypothesis that its shape is topologically equivalent to a filled sphere as shown in Fig. 1 (right). The segmentation is performed as follows:

1. Extract an inner object (C_{inner}) that is within the whole CSF as close as possible to its actual borders and has the same topology.
2. Extract an outer object of the CSF (C_{lim}) that includes the whole CSF but do not necessarily have the same topology.
3. Homotopically thicken C_{inner} preserving its topology as long as it remains within C_{lim} . The transformation is guided by a priority function based on a distance criterion.

Note that obtaining both, inner and outer objects, as close as possible to the object of interest, allows to speed up significantly the processing time.

2.1 Extraction of an inner object of the CSF

An inner object is extracted by applying the moment-preserving thresholding described in [33] on the initial image followed by a larger connected component extraction (Fig. 4–b).

2.1.1 Moment-preserving thresholding

This method is suited to “binary nature” images with a low contrast. When the histogram presents an excessive overlapping between classes, the moment-preserving method becomes more efficient than conventional clustering-based or entropy-based methods.

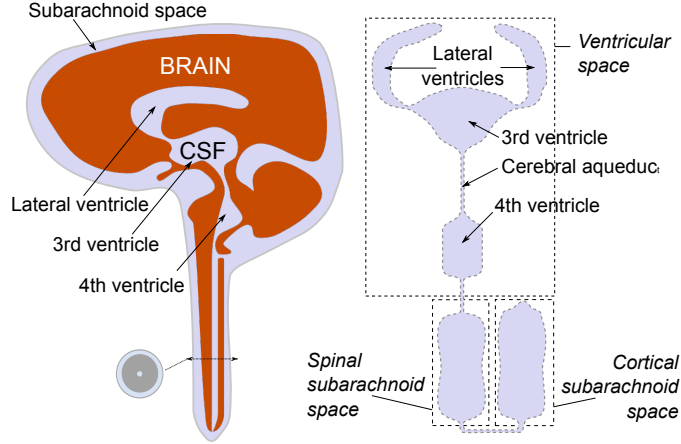


Figure 1: The CSF around the brain is considered as topologically equivalent to a filled sphere (right). In an axial cross-section of the spinal chord, the CSF has a disk topology (left).

The moment preservation assumes that statistical moments on original and thresholded images are identical. Let $F = \{f_{ijk}\}$ be a 3D image of L intensity levels. For each intensity level z , its associated normalized histogram is given by $p(z)$ and the statistical moment M of order m for $m = 1, 2, 3$ is defined as: $M_m = \sum_{z=0}^{L-1} p(z) z^m$.

The resulting thresholded image $G = \{g_{ijk}\}$ may be considered to be composed of two gray levels z_0 and z_1 ($z_0 < z_1$). The optimal threshold T_{inner} is obtained such that first three moments for F , the mean M_1 , the variance M_2 and the skewness M_3 , are equals to those for G when $g_{ijk} = z_0$ (resp. $g_{ijk} = z_1$) if $f_{ijk} \leq T_{\text{inner}}$ (resp. $f_{ijk} > T_{\text{inner}}$).

Let P_0 and P_1 be the percentages of voxels of G on both sides of T_{inner} , the statistical moment B_m of order m is: $B_m = \sum_{l=0}^1 P_l z_l^m$. Moments preservation leads to solve the system:

$$\sum_{l=0}^1 P_l z_l^m = \sum_{z=0}^{L-1} p(z) z^m, \quad (1)$$

with the constraint $P_0 + P_1 = 1$ for $m = 1, 2, 3$. Equation (1) has four unknowns z_0 , z_1 , P_0 and P_1 , whose solution can be found in [33] and leads to a value for T_{inner} that is given by:

$$P_0 = \frac{1}{L} \sum_{z=1}^{T_{\text{inner}}} p(z). \quad (2)$$

Figure 2 shows an histogram with the threshold T_{inner} ($= 38$) obtained from the moment-preserving method, which allows to retrieve the inner CSF. T_{lim} ($= 13$) is the threshold using the triangle thresholding, which is presented in Section 2.2 and allows to retrieve the outer object of the CSF. For comparison, the Otsu threshold T_{Otsu} ($= 53$) is also shown.

In Tab. 1, the results obtained by the other thresholding methods reviewed in [31], for the histogram on Fig. 2, are also presented for comparison to that of the moment-preserving and result in more distant threshold values.

2.1.2 Retrieval of the inner object

Since G contains several thresholded objects, a connected component labeling is performed to extract the three largest connected components (the inner object C_{inner} and both eyeballs E_1 and

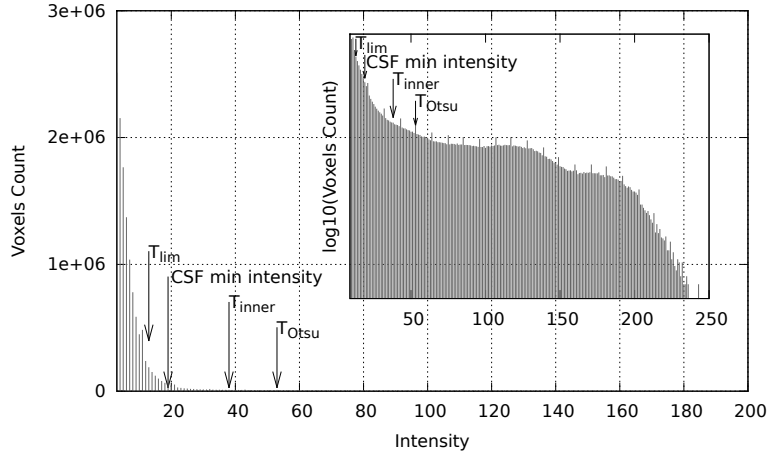


Figure 2: Image histogram sample from the clinical dataset and its zooming (vertical log scale) at the upper-right corner.

Table 1: Threshold values obtained on the histogram from Fig. 2 using various methods also reviewed in [31].

Method	Threshold
Attribute_Huang [10]	1
Cluster_Kittler [12]	5
Cluster_Ridler [24]	52
Entropy_Kapur [11]	43
Entropy_Li [15]	4
Entropy_Sahoo [26]	43
Entropy_Shanbag [32]	241
Entropy_Yen [35]	53

E_2). E_1 and E_2 are retained to determine a region of interest in Section 3.1. If C_{inner} has holes, then T_{inner} is automatically adjusted by increasing its value until the topological assumption is satisfied (E_1 and E_2 are not affected by this operation due to their intensity). By extracting the largest components (Fig. 4-b), residual noise as well as other small objects such as salivary ducts are also removed.

2.2 Thresholding of an outer object of the CSF

To extract an outer object of the CSF, another histogram-based thresholding method is carried out on the initial image as described in [36]. It is followed by a largest connected component extraction to retrieve an outer object of the CSF (C_{lim}).

The triangle thresholding algorithm in [36] is suitable for bimodal images for which the object to extract has a small amplitude and a large variance relatively to the background. Let $p(z)$ be the histogram function for gray levels z . Maximum and minimum values, p_{max} and p_{min} , are determined from $p(z)$ with their z values, z_{min} and z_{max} , and the points $(z_{\text{min}}, p_{\text{min}})$ and $(z_{\text{max}}, p_{\text{max}})$ are connected by a line segment δ . Let $d_e(a, b)$ be the Euclidean distance between two points a and b . For each point $a = (z, p(z))$, we can define the minimum distance from the

line segment δ such that: $d_{\min}(z, p(z)) = \min_{b \in \delta} \{d_e(a, b)\}$. The optimal threshold T_{lim} is obtained such that:

$$T_{\text{lim}} = \underset{z}{\operatorname{argmax}} \{d_{\min}(z, p(z))\}. \quad (3)$$

C_{lim} is the object obtained as the largest connected component of the thresholded image.

2.3 Homotopic thickening of the inner object

An homotopic thickening is carried out on the inner object C_{inner} . The thickening is guided by a priority function Ψ that is related to C_{lim} and based on a distance criterion.

2.3.1 Priority function

The priority function $\Psi = \{\psi_{ijk}\}$ controls the order in which voxels are processed and eventually added to C_{inner} . This function uses an Euclidean distance map denoted by $D = \{d_{ijk}\}$, which is calculated by the linear algorithm proposed in [27]. The value ψ_{ijk} of each voxel (i, j, k) in the outer object C_{lim} is its distance to the nearest non-zero voxel of C_{inner} such that:

$$\psi_{ijk} = \begin{cases} d_{ijk} & \text{if } (i, j, k) \in C_{\text{lim}} \\ +\infty & \text{otherwise.} \end{cases} \quad (4)$$

2.3.2 Guided homotopic thickening

Guided by the previous priority function Ψ , an homotopic thickening is applied to the inner object C_{inner} by adding simple points.

A point is simple if its addition to or its removal from a binary object C does not change the topology of the object and of the background. Therefore, removing simple points does not change the number of connected components and holes (cavities and/or tunnels) of C and its complement \bar{C} . It is shown in [3] that a simple point x is locally characterized by two topological numbers denoted by $\mathcal{T}_n(x, C)$ and $\mathcal{T}_{\bar{n}}(x, \bar{C})$ for $(n, \bar{n}) \in \{(6, 26), (26, 6)\}$, such that $\mathcal{T}_n(x, C) = 1$ and $\mathcal{T}_{\bar{n}}(x, \bar{C}) = 1$. An efficient computation of $\mathcal{T}_n(x, C)$ and $\mathcal{T}_{\bar{n}}(x, \bar{C})$ that only involves the 26-neighborhood is also described in [3].

Let $\partial\bar{C}_{\text{inner}}$ denotes the boundary of C_{inner} such that $\partial\bar{C}_{\text{inner}} = \{x \in (\bar{C}_{\text{inner}} \cap C_{\text{lim}}) \mid N_n(x) \cap C_{\text{inner}} \neq \emptyset\}$, where \bar{C}_{inner} is the complement of C_{inner} and $N_n(x)$ is the n -neighborhood of x with $n \in \{6, 26\}$. The thickening process consists to add to C_{inner} simple points from $\partial\bar{C}_{\text{inner}}$ as presented in Algorithm 1. It shows that boundary points (i.e. voxels) of $\partial\bar{C}_{\text{inner}}$ are chosen iteratively, according to their priorities, and are incorporated into C_{inner} if they are simple. The resulting thickened object is illustrated in Fig. 3-d and 4-c, d.

3 Separation into CSF volumes

The separation of the CSF spaces is required to analyze the relationship between the ventricular and intracranial subarachnoid volumes. First, the spinal and intracranial regions are separated using geometrical and topological properties of the CSF at their interface. Second, to retrieve the ventricular space volume from that of the intracranial subarachnoid one, the cerebral aqueduct must be detected because we use it as a morphological reconstruction marker.

Algorithm 1: Guided homotopic thickening

Input: C_{inner}, Ψ **Output:** C_{inner} Make a priority queue \mathcal{Q} from $\partial\bar{C}_{\text{inner}}$ using ψ_{ijk} in the ascending order**while** $\mathcal{Q} \neq \emptyset$ **do** Poll $x = (i, j, k)$ from \mathcal{Q} ; **if** x is simple for C_{inner} **then** $C_{\text{inner}} \leftarrow C_{\text{inner}} \cup \{x\}$; Add new points of $\partial\bar{C}_{\text{inner}}$ around x to \mathcal{Q} ; **end if****end while**

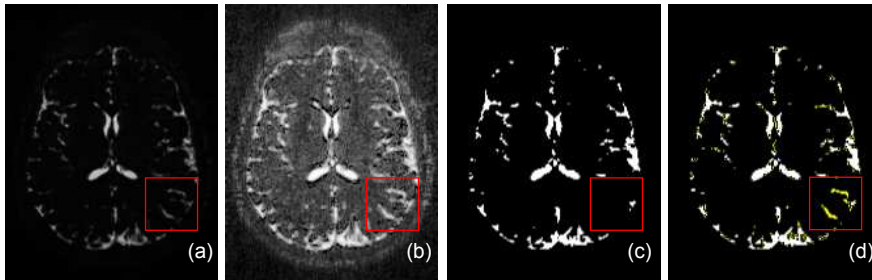


Figure 3: Segmentation process (axial cross-section), which is easily observed in the red square region. (a) original image; (b) contrast-enhanced original image; (c) inner object image; (d) homotopic thickened image.

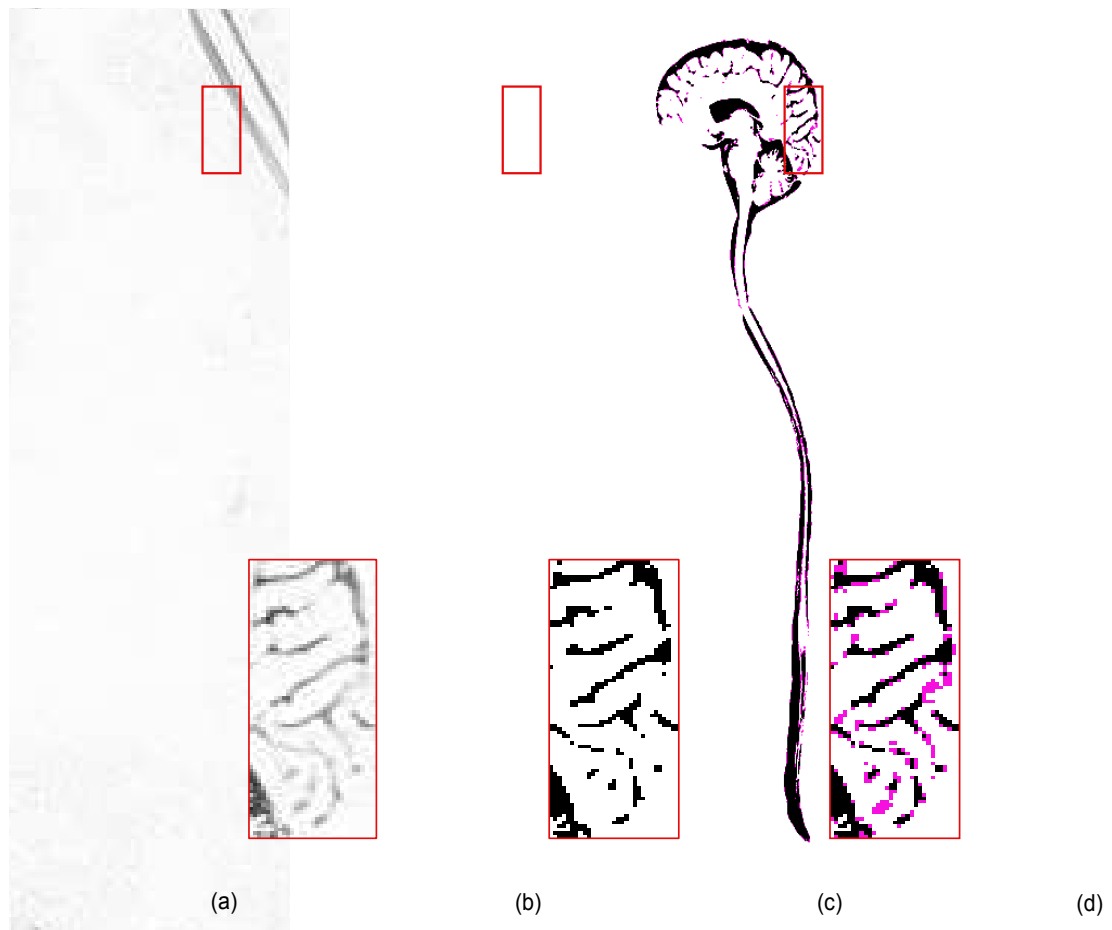


Figure 4: Segmentation process (sagittal cross-section). In each figure, the red rectangular region is zoomed in the bottom for more details. (a) original image; (b) inner object image; (c) homotopic thickened image; (d) 3D reconstruction after thickening. [inverted grayscale used to improve printing]

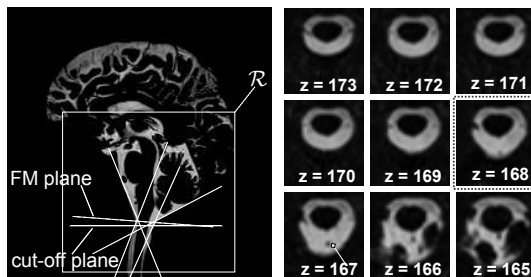


Figure 5: Separation of intracranial and spinal regions in the ROI \mathcal{R} . The resulting cut-off plane ($z = 168$) is close to that goes through the foramen magnum (FM plane). The axial cross-sections around the cut-off plane are also illustrated (right).

3.1 Separation of spinal and intracranial spaces

Expert physicians usually perform the disconnection of the spinal and intracranial spaces by tracking the foramen magnum (the hole in the bottom of the skull through which the spinal cord passes in order to be connected to the brain), which is even for an expert, difficult to detect on this type of images. The separation into spinal and intracranial spaces requires to locate the closest axial cross-section plane to that of the foramen magnum. Thus, the disconnection is achieved by browsing the 2D connected component on each axial plane from the spinal part, and by detecting any change in its topology (see the axial cross-section in Fig. 5). A region of interest (ROI) is first determined to reduce the processing time as well as to improve the robustness.

3.1.1 Determination of the ROI

An ROI \mathcal{R} is used on one hand to locate the cutting axial cross-section, and on the other hand to retrieve the cerebral aqueduct in order to separate the intracranial space into its ventricular and subarachnoid spaces (Section 3.2). Apart from pathological cases, the eyeballs typically face the cerebral aqueduct in the axial plane. We consider the ROI forming a rectangular cuboid, each of whose edge is parallel to one of the i -, j -, k -axes of the image and such that:

- The ROI is located in the i -axis direction between the coronal plane that passes through the maximum posterior boundary of E_1 and E_2 , and the last coronal plane that still contains non-zero voxels.
- Let D be the larger diameter of E_1 and E_2 . The height of the ROI is set empirically to be $8D$, such that the top face of the ROI is located with the distance $2D$ above the eyeballs and the bottom face is located with the distance $5D$ below the eyeballs. The height may be interactively resized to fit human variations.
- The depth is determined by the two sagittal planes between the medial boundaries of E_1 and E_2 .

3.1.2 Determination of the cut-off plane

2D connected components are counted on each axial plane from the bottom to the top of the ROI \mathcal{R} . The first axial plane that shows a change in the topology of the connected components is the plane just above that of the searched cut-off (Fig. 5).

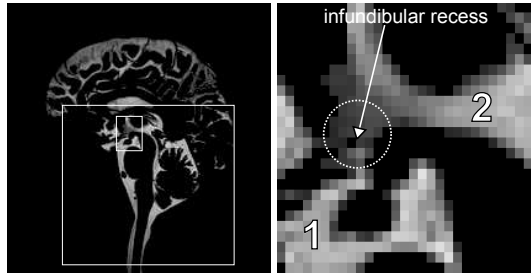


Figure 6: Proximity of the interpeduncular cistern (1) to the infundibular recess of the third ventricle (2). The small rectangular part in the left figure is zoomed in the right figure.

3.2 Intracranial volumes separation

The process to extract the ventricular space may fail because of some subarachnoid regions that are very close to the third and fourth ventricles. Figure 6 shows, for instance, the proximity between the interpeduncular cistern and the infundibular recess of the third ventricle.

To overcome this problem we first detect a specific tubular object. The cerebral aqueduct is a thin tubular structure (diameter: 1 to 3 mm; length: ~ 14 mm) located in the median sagittal plane, which connects the third and fourth ventricles. It is also the longest tubular structure with the highest intensity range in the most median sagittal planes of the ROI \mathcal{R} . Its enhancement is performed by a vessel segmentation method (see [14]). Finally, ventricles are recovered by a morphological reconstruction [34] using the cerebral aqueduct as a marker.

3.2.1 Detection of the cerebral aqueduct

Several methods to enhance vessel-like structures in 2D and 3D grayscale images are reviewed in [14]. Some efficient methods are based on properties of eigenvalues of the Hessian matrix \mathcal{H} [17, 28, 7, 13, 19]. These multi-scale methods operate in a Gaussian scale space on which they calculate second-order derivatives, build the Hessian matrix \mathcal{H} , and decompose it depending on its eigenvalues λ_1 , λ_2 and λ_3 such that $|\lambda_1| < |\lambda_2| < |\lambda_3|$. The eigenvalues are analyzed to determine the likelihood for each voxel (i, j, k) to belong to a curvilinear structure. This analysis is based on the following assumptions: 1) $\lambda_1 \approx 0$; 2) $\lambda_2 \approx \lambda_3 < 0$; and 3) $|\lambda_1| \ll |\lambda_2|$.

The tubular structure filter implemented in [7] is used to enhance the cerebral aqueduct. Let $F_\sigma = \{f_{ijk}^\sigma\}$ the filter in [7] such that:

$$f_{ijk}^\sigma = \begin{cases} 0 & \text{if } \lambda_2 > 0 \text{ or } \lambda_3 > 0, \\ (1 - e^{-\frac{\mathcal{R}_A^2}{2\alpha^2}})e^{-\frac{\mathcal{R}_B^2}{2\beta^2}}(1 - e^{-\frac{\mathcal{S}^2}{2c^2}}) & \text{otherwise,} \end{cases} \quad (5)$$

where $\mathcal{R}_A = |\lambda_2| / |\lambda_3|$, $\mathcal{R}_B = |\lambda_1| / \sqrt{|\lambda_2\lambda_3|}$, $\mathcal{S} = \sqrt{\lambda_1^2 + \lambda_2^2 + \lambda_3^2}$, with some weights $\alpha \in [0, 1]$, $\beta \in [0, 1]$ and $c \in [0, 500]$. Figure 7 compares extracted curvilinear structures in the ROI \mathcal{R} using methods from [28] (Fig. 7-b) and [7] (Fig. 7-c). It shows that unlike the filter in [28], that in [7] allows to dissociate strict tubular structures from others. The cerebral aqueduct part has more highlighted values in Fig. 7-c by adjusting the filter with a higher weight to detect lines ($\alpha = 0.7$). The aqueduct is the longest connected component found in the most median sagittal planes.

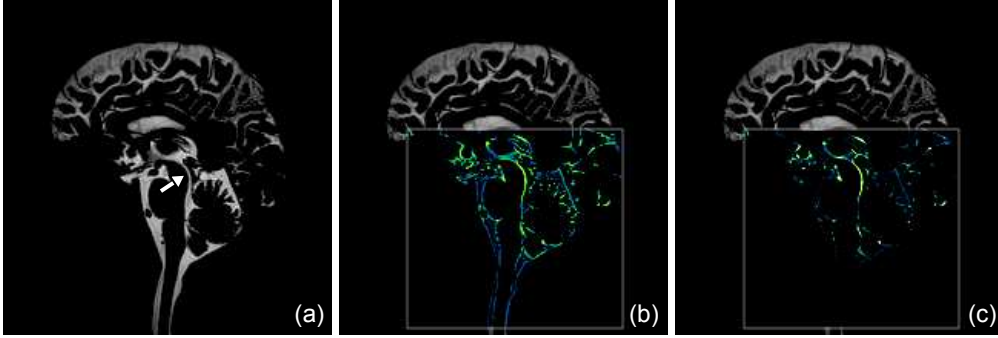


Figure 7: Detection of the cerebral aqueduct in the ROI \mathcal{R} (median plane cross-section). From left to right: (a) original thickened image; (b) filtered image by [28] ($\sigma = 0.5$); (c) filtered image by [7] using 5 scale spaces σ from 0.4 to 0.9 and with $\alpha = 0.7$, $\beta = 0.2$ and $c = 200$.

3.2.2 Ventricles reconstruction

Considering the cerebral aqueduct part as the marker, we would like to reconstruct all the ventricles. For this problem, methods such as fast marching [30], level set [30] or active contour models [4] are well known. However, the following two problems may hinder the reconstruction by the above methods: 1) the cerebral aqueduct part is too small as a marker to initialize a model; 2) motion artifacts may generate significant intensity inhomogeneities even in the ventricular spaces.

Grayscale reconstruction [34] is a very useful operator from mathematical morphology that provides satisfactory results here. Let $\delta_{f,B_d}^{(1)}(g)$ be the elementary geodesic dilation of a grayscale image g inside f (g is called the marker image and f is the mask) such that $\delta_{f,B_d}^{(1)}(g) = (g \oplus B_d) \wedge f$, where \wedge stands for the point-wise minimum and $g \oplus B_d$ is the geodesic dilation of g by an isotropic structuring element B_d chosen as the unit ball. The geodesic dilation of size $n \geq 0$ is obtained by:

$$\delta_{f,B_d}^{(n)}(g) = \underbrace{\delta_{f,B_d}^{(1)} \circ \delta_{f,B_d}^{(1)} \circ \dots \circ \delta_{f,B_d}^{(1)}}_{n \text{ times}}(g). \quad (6)$$

The grayscale reconstruction by dilation $\rho_{f,B_d}(g)$ of f from g is calculated by iterating geodesic dilations of g inside f until idempotence such that:

$$\rho_{f,B_d}(g) = \bigvee_{n \geq 1} \delta_{f,B_d}^{(n)}(g), \quad (7)$$

where \bigvee stands for the point-wise maximum.

The ventricular space volume is retrieved by dilation of the previously detected cerebral aqueduct used as the marker image, using the parallel reconstruction algorithm proposed in [34]. Figure 8 shows the result of such a reconstruction using a 6-connectivity.

4 CSF volumes analysis

As the ground truth is not available for clinical data, the segmentation method for the total volume assessment was first validated on phantom MR images. Experiments were carried out on four phantoms of known volume (image size: $250 \times 250 \times 128$ voxels) and 17 clinical MR images (image size: $\sim 260 \times 790 \times 160$ voxels).

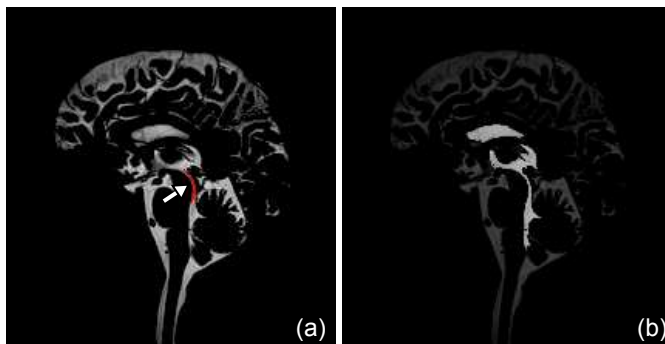


Figure 8: Ventricular space retrieving using a grayscale reconstruction by dilation of the cerebral aqueduct inside the original image: (a) the original image (the mask) and the cerebral aqueduct (the marker) colored in red; (b) result of the grayscale reconstruction.

4.1 Images acquisition

MR images were acquired in the sagittal plane on a 1.5 T system (Magnetom Avanto; Siemens Medical Solutions, Erlangen, Germany). The MR sequence in [9], called SPACE (Sampling Perfection with Application optimized Contrast using different flip-angle Evolution), is a variant of the T2-weighted turbo spin echo sequence with variable flip-angles. The sequence was as follows: repetition time TR (ms)/echo time TE (ms), 2400/762; turbo factor of 141; 250×250 mm field of view; 256×256 acquisition matrix; 1 mm isotropic resolution; number of excitations 1.4; 160 slices; acquisition time, 3 min [9].

4.2 Complexity and computation time

The complexity in time is dominated by the homotopic thickening step and is $\mathcal{O}(n \log n)$ where n is the number of points in $\bar{C}_{\text{inner}} \cap C_{\text{lim}}$. It may be reduced to be linear by parallelizing the homotopic thickening process. The total computation time for segmentation and separation was performed from 3 to 6 minutes on an Intel Pentium Dual Core 1.60 GHz / 2 GB for each clinical MR image.

4.3 Validation on phantoms

Images were acquired from blood bags and synthetic resin phantoms with various shapes and volumes (see an example in Fig. 9). Phantoms 1 and 2 have regular shape while phantoms 3 and 4 have more tortuous one.

It has been observed (Fig. 10) that both segmentations, the semi-manual by an expert as explained in [9] and the grayscale reconstruction [34], have resulted in an overestimation. Instead, the methods of homotopic thickening and level set initialized by a fast marching have produced underestimated but close results. The guided homotopic thickening on phantoms has resulted in an accuracy of $98.5\% \pm 1.8$ against $94.6\% \pm 4.0$ for the semi-manual segmentation by an expert.

4.4 Statistical analysis on clinical data

Clinical images were acquired from different subjects (ages between 25 and 84 years): seven healthy volunteers, two patients with a communicating hydrocephalus just two days after their surgery, and eight patients among which seven communicating hydrocephalus (CH) and one

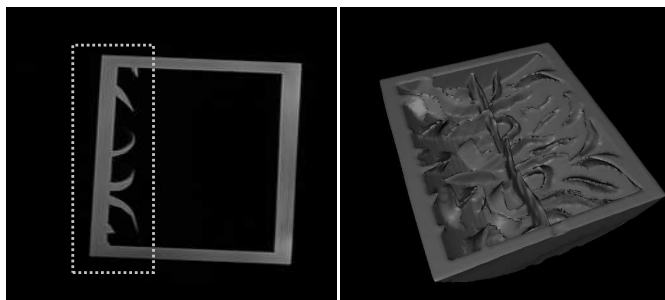


Figure 9: Example of a synthetic resin phantom MR image. Cross-section of the phantom (left). The 3D reconstruction of the rectangular region is shown in the right figure.

non-communicating hydrocephalus (NCH). Due to the limited number of clinical images, the CH and NCH patients have not been distinguished. In addition, the two patients who just have undergone their surgery were removed from the analysis because according to physicians, the CSF has not had enough time to reach the whole subarachnoid space.

4.4.1 Classification of clinical data

Following the proposal in [9] to use ratios to classify data, a linear discriminant analysis [6] was first performed on the clinical dataset using volumes of the ventricular and intracranial subarachnoid spaces as the input variables. Let TP , FP , TN and FN the respective numbers of true positives, false positives, true negatives and false negatives. The sensitivity S_e and the specificity (or recall) S_p are respectively defined as $S_e = TP/(TP+FN)$ and $S_p = TN/(TN+FP)$. The additional F_1 -score metric is also used to validate the classifier. It is defined as $F_1 = 2pS_e/(p + S_e)$ where p stands for the precision, defined by $p = TP/(TP + FP)$. The predicted classification on the clinical data results in a sensitivity/specificity/ F_1 -score of 100%, which is a suitable result to discriminate between healthy people and pathological cases (Fig. 11). A similar observation was made on data from [9].

This first result appears to confirm such as in [9] that the relationship between the ventricular CSF space volume and the intracranial subarachnoid could be an efficient functional parameter to distinguish healthy people from pathological cases.

4.4.2 Linear regression model for healthy adults

Observing the previous result has provided us the idea of carrying out a linear regression on the healthy people subset that results from the linear discriminant analysis step. Let V_V and V_S the respective volumes of the ventricular and intracranial subarachnoid spaces. We use the linear model: $V_S = \beta_0 + \beta_1 V_V + \epsilon$, and optimize the intercept β_0 and the slope β_1 by minimizing the residual error ϵ . We obtain $\beta_0 = 0$ and $\beta_1 = 0.1071$, namely:

$$V_V = 0.1071V_S \quad (8)$$

Table 2 includes some statistics about the model: 1) the coefficient of determination R^2 (= 98.43%) indicates that the predictor explains rather well the answer; 2) the F statistic (= 312.8) and the p -value (= $1.06e-05 \ll 0.05$) show further that the null hypothesis ($\beta_1 = 0$) can be rejected with a strong presumption. In addition, the graphical residuals analysis reinforces the linear regression assumptions (Fig. 12).

Table 2: Optimal linear regression model from the clinical data set.

Model	R^2	σ^2	Standard Error	F	p -value
$V_V = 0.1071V_S$	0.9843	12.25	0.0061	312.8	1.06e-05

The left figure of Fig. 13 shows the distribution of ventricular and intracranial subarachnoid volumes with the model obtained from (8). The right figure illustrates the same model with the distribution of the data from [9].

5 Conclusion

This work uses a new sequence of whole body MRI and succeeds in providing good estimations of the volumes of the CSF. The volumes are automatically retrieved through segmentation and separation steps, which use image properties, anatomical and geometrical features, as well as topological assumptions on the CSF. The proposed method seems to confirm the assumption that the proportional relationship between the ventricular and intracranial subarachnoid volumes allows to discriminate healthy and pathological cases. As the database is currently in expansion, our tool facilitates the refinement of these results in future work.

This new ability to quantify CSF volumes, which is a main parameter for the diagnosis, for the treatment decisions, for the monitoring of patients, and finally for clinical research, may represent an important breakthrough in the field of computer-aided neuro-imaging.

References

- [1] Pierre-Louis Bazin and Dzung L. Pham. Topology-preserving tissue classification of magnetic resonance brain images. *IEEE Transactions on Medical Imaging*, 26(4):487–496, 2007.
- [2] Pierre-Louis Bazin and Dzung L. Pham. Homeomorphic brain image segmentation with topological and statistical atlases. *Medical Image Analysis*, 12(5):616–625, 2008.
- [3] Gilles Bertrand and Grégoire Malandain. A new characterization of 3-dimensional simple points. *Pattern Recognition Letters*, 15:169–175, 1994.
- [4] Laurent D. Cohen. On active contours models and balloons. *Computer Vision, Graphics, and Image Processing: Image Understanding*, 53(2):211–218, 1991.
- [5] Petr Dokládál, Isabelle Bloch, Michel Couprie, Daniel Ruijters, Raquel Urtasun, and Line Garnero. Topologically controlled segmentation of 3D magnetic resonance images of the head by using morphological operators. *Pattern Recognition*, 36(10):2463–2478, 2003.
- [6] Richard O. Duda, Peter E. Hart, and David G. Stork. *Pattern Classification*. Wiley Interscience, 2nd edition, 2000.
- [7] Alejandro F. Frangi, Wiro J. Niessen, Koen L. Vincken, and Max A. Viergever. Multiscale vessel enhancement filtering. In *MICCAI 1998*, volume 1496 of *Lecture Notes in Computer Science*, pages 130–137, Cambridge MA, USA, 1998. Springer.

- [8] Xiao Han, Chenyang Xu, and J.L. Prince. Topology preserving level set method for geometric deformable models. *IEEE Transactions on Pattern Analysis and Machine Intelligence*, 25(6):755–768, 2003.
- [9] Jérôme Hodel, Jonathan Silvera, Olivier Bekaert, Alain Rahmouni, Sylvie Bastuji-Garin, Alexandre Vignaud, Eric Petit, Bruno Durning, and Philippe Decq. Intracranial cerebrospinal fluid spaces imaging using a pulse-triggered three-dimensional turbo spin echo MR sequence with variable flip-angle distribution. *European Radiology*, 21(2):402–410, 2011.
- [10] Liang-Kai Huang and Mao-Jiun J. Wang. Image thresholding by minimizing the measures of fuzziness. *Pattern Recognition*, 28(1):41–51, 1995.
- [11] J.N. Kapur, P.K. Sahoo, and A.K.C. Wong. A new method for gray-level picture thresholding using the entropy of the histogram. *Graphical Models and Image Processing*, 29(3):273–285, 1985.
- [12] J. Kittler and J. Illingworth. Minimum error thresholding. *Pattern Recognition*, 19(1):41–47, 1986.
- [13] Karl Krissian, Grégoire Malandain, and Nicholas Ayache. Model based detection of tubular structures in 3D images. *Computer Vision and Image Understanding*, 80(2):130–171, 2000.
- [14] David Lesage, Elsa D. Angelini, Isabelle Bloch, and Gareth Funka-Lea. A review of 3D vessel lumen segmentation techniques: Models, features and extraction schemes. *Medical Image Analysis*, 13(6):819–845, 2009.
- [15] C.H. Li and P.K.S. Tam. An iterative algorithm for minimum cross entropy thresholding. *Pattern Recognition Letters*, 19(8):771–776, 1998.
- [16] Andreas A. Linninger, Michalis Xenos, David C. Zhu, MahadevaBharath R. Somayaji, Srinivasa Kondapalli, and Richard D. Penn. Cerebrospinal fluid flow in the normal and hydrocephalic human brain. *IEEE Transactions on Bio-Medical Engineering*, 54(2):291–302, 2007.
- [17] C. Lorenz, I.-C. Carlsen, T. M. Buzug, C. Fassnacht, and J. Weese. Multi-scale line segmentation with automatic estimation of width, contrast and tangential direction in 2D and 3D medical images. In *CVRMed-MRCAS’97*, volume 1205 of *Lecture Notes in Computer Science*, pages 233–242, London, UK, 1997. Springer.
- [18] J.-F. Mangin, V. Frouin, I. Bloch, J. Régis, and J. Lopez-Krahe. From 3D magnetic resonance images to structural representations of the cortex topography using topology preserving deformations. *Journal of Mathematical Imaging and Vision*, 5(4):297–318, 1995.
- [19] Rashindra Manniesing, Max A. Viergever, and Wiro J. Niessen. Vessel enhancing diffusion: A scale space representation of vessel structures. *Medical Image Analysis*, 10:815–825, 2006.
- [20] Sanae Miri, Nicolas Passat, and Jean-Paul Armspach. Topology-preserving discrete deformable model: Application to multi-segmentation of brain MRI. In *3rd International Conference on Image and Signal Processing (ICISP 2008)*, volume 5099 of *Lecture Notes in Computer Science*, pages 67–75, Cherbourg-Octeville, France, 2008. Springer.
- [21] A. Peña, N.G. Harris, M.D. Bolton, M. Czosnyka, and J.D. Pickard. Communicating hydrocephalus: The biomechanics of progressive ventricular enlargement revisited. *Acta Neurochir*, 81:59–63, 2002.

- [22] F. Poupon, J.-F. Mangin, D. Hasboun, C. Poupon, I. Magnin, and V. Frouin. Multi-object deformable templates dedicated to the segmentation of brain deep structures. In *MICCAI 1998*, volume 1496 of *Lecture Notes in Computer Science*, pages 1134–1143, Cambridge MA, USA, 1998. Springer.
- [23] Harold L. Rekate. A contemporary definition and classification of hydrocephalus. *Seminars in Pediatric Neurology*, 16(1):9–15, 2009.
- [24] T. W. Ridler and S. Calvard. Picture thresholding using an iterative selection method. *IEEE Transactions on Systems, Man and Cybernetics*, 8(8):630–632, 1978.
- [25] Andrea Rueda, Oscar Acosta, Michel Couprie, Pierrick Bourgeat, Jurgen Fripp, Nicholas Dowson, Eduardo Romero, and Olivier Salvado. Topology-corrected segmentation and local intensity estimates for improved partial volume classification of brain cortex in MRI. *Journal of Neuroscience Methods*, 188(2):305–315, May 2010.
- [26] Prasanna Sahoo, Carrye Wilkins, and Jerry Yeager. Threshold selection using renyi’s entropy. *Pattern Recognition*, 30(1):71–84, 1997.
- [27] Toyofumi Saito and Jun-Ichiro Toriwaki. New algorithms for euclidean distance transformation on an N-dimensional digitized picture with applications. *Pattern Recognition*, 27(11):1551–1565, 1994.
- [28] Yoshinobu Sato, Shin Nakajima, Hideki Atsumi, Thomas Koller, Guido Gerig, and Shigeyuki Yoshida. Three-dimensional multi-scale line filter for segmentation and visualization of curvilinear structures in medical images. *Medical Image Analysis*, 2(2):143–168, 1998.
- [29] Florent Ségonne. *Segmentation of Medical Images under Topological Constraints*. PhD thesis, Massachusetts Institute of Technology, Cambridge MA, USA, 2005.
- [30] James A. Sethian. *Level Set Methods and Fast Marching Methods: Evolving Interfaces in Computational Geometry, Fluid Mechanics, Computer Vision, and Materials Science*. Cambridge University Press, 1999.
- [31] Mehmet Sezgin and Bülent Sankur. Survey over image thresholding techniques and quantitative performance evaluation. *Journal of Electronic Imaging*, 13(1):146–165, 2004.
- [32] A.G. Shanbag. Utilization of information measure as a means of image thresholding. *Graphical Models and Image Processing*, 56(5):414–419, 1994.
- [33] Wen-Hsiang Tsai. Moment-preserving thresholding: a new approach. *Computer Vision, Graphics, and Image Processing*, 29:377–393, 1985.
- [34] Luc Vincent. Morphological grayscale reconstruction in image analysis: Applications and efficient algorithms. *IEEE Transactions on Image Processing*, 2(2):176–201, 1993.
- [35] J. C. Yen, F. J. Chang, and S. Chang. A new criterion for automatic multilevel thresholding. *IEEE Transactions on Image Processing*, 4(3):370–378, 1995.
- [36] G. W. Zack, W. E. Rogers, and S. A. Latt. Automatic measurement of sister chromatid exchange frequency. *Journal of Histochemistry and Cytochemistry*, 25(7):741–753, 1977.

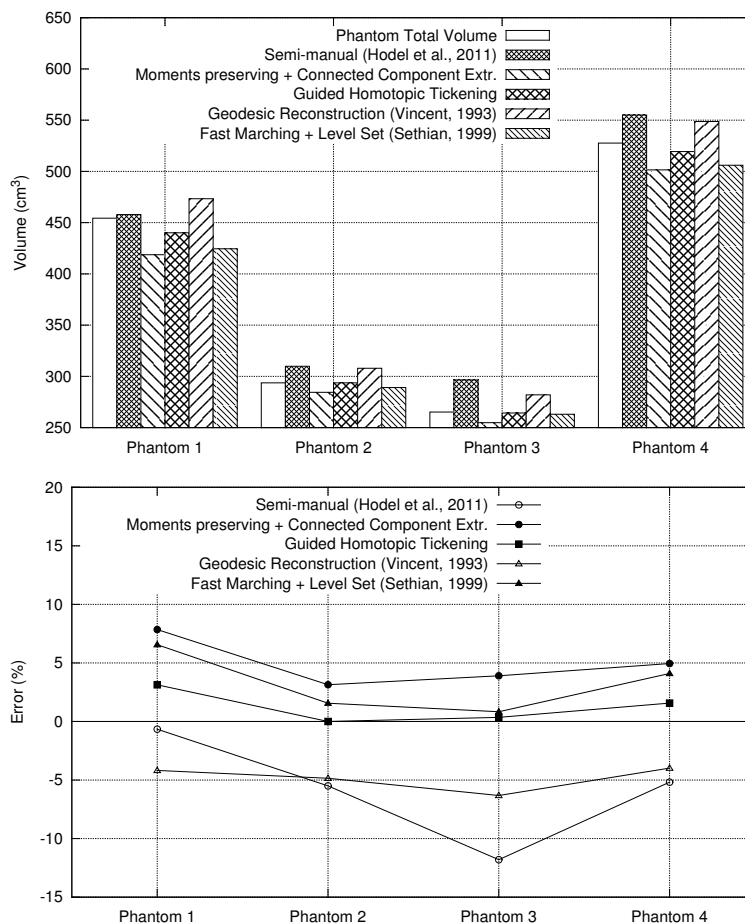


Figure 10: Comparisons of the total volume assessment of phantoms for different methods. Top: total volume measurement for objects that result from: the semi-manual segmentation by an expert as described in [9]; the initial inner object extraction (Section 2.1); the homotopic thickening process (Section 2.3); a grayscale reconstruction method [34] and a fast marching followed by a level set method [30], both using the inner object as a marker. Bottom: errors on the total volume measurement for the previous methods.

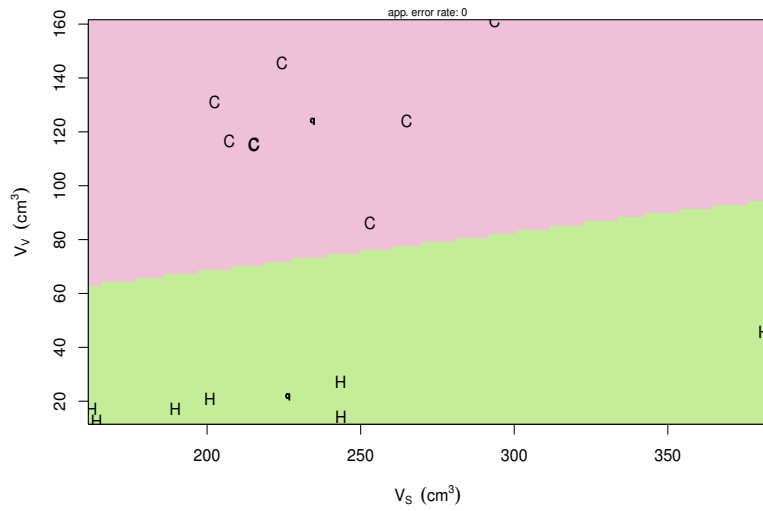


Figure 11: Resulting partition plots on clinical data by using a linear discriminant analysis considering two classes: “Healthy (H) and Pathological (C)”.

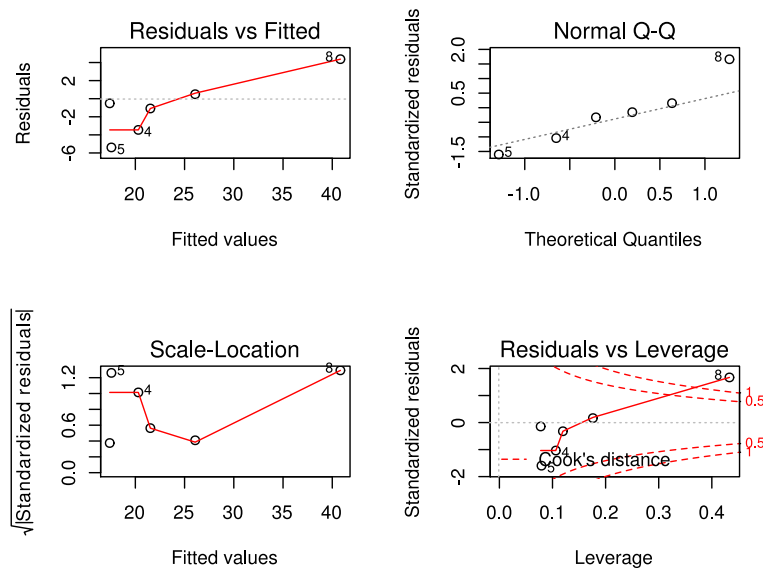


Figure 12: Residual plots from the linear regression on clinical data.

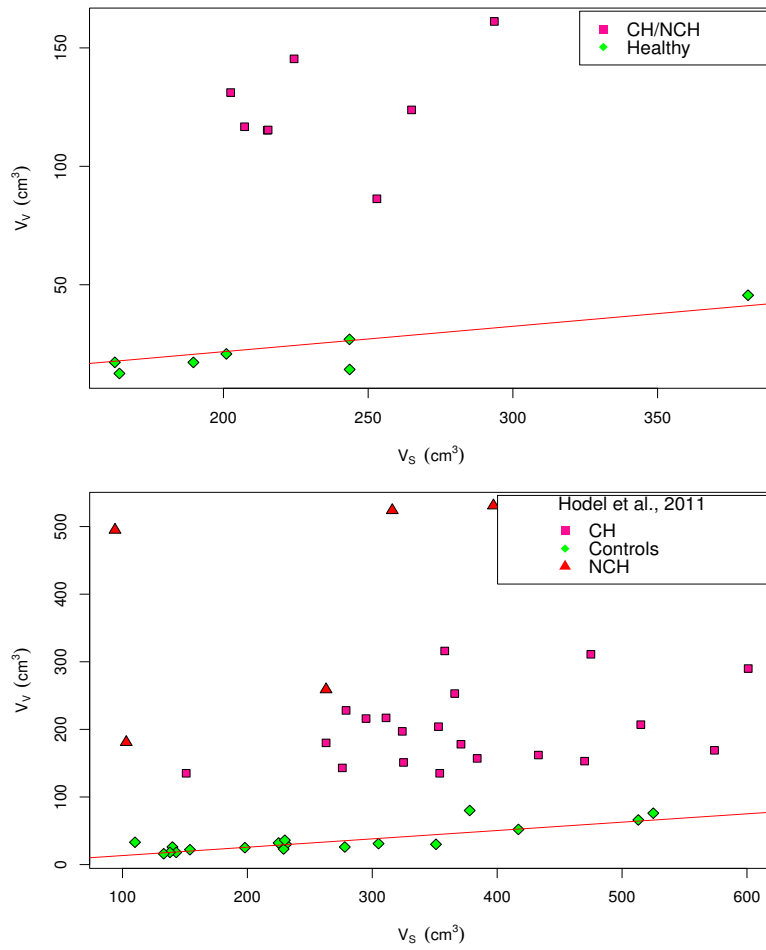


Figure 13: Linear model on $V_V \sim V_S$ distributions. Top: the resulting linear regression on the healthy people subset of the clinical dataset; bottom: the linear model fitted on the healthy people subset of the dataset from [9].